Contrasting Aerosol Mixing States at Inland and Coastal Sites: An Entropy-Based Metric for CCN Activity

Jingye Ren[1,2], Wei Xu[3], Ru-Jin Huang[1*], Fang Zhang[4*], Ying Wang[1], Lu Chen[5], Jurgita Ovadnevaite[6], Darius Ceburnis[6], Colin O'Dowd[6], Yele Sun[7]

[1]*State Key Laboratory of Loess Science, Institute of Earth Environment, Chinese Academy of Sciences, Xi'an, 710061, China,*

[2]*Xi'an Institute for Innovative Earth Environment Research, Xi'an, 710061, China,*

[3]*State Key Laboratory of Advanced Environmental Technology, Institute of Urban Environment, Chinese Academy of Sciences, Xiamen, 361021, China,*

[4]*School of Ecology and Environment, College of Artificial Intelligence, Harbin Institute of Technology, Shenzhen, 518005, China,*

[5]*School of Ocean and Geographic Science, Yancheng Teachers University, Yancheng 224051, China,*

[6]*School of Natural Sciences, Centre for Climate & Air Pollution Studies, Ryan Institute, University of Galway, University Road, Galway, Ireland,*

[7]*State Key Laboratory of Atmospheric Boundary Layer Physics and Atmospheric Chemistry, Institute of Atmospheric Physics, Chinese Academy of Sciences, Beijing 100029, China.*

Corresponding author: Ru-Jin Huang, *rujin.huang@ieecas.cn;* Fang Zhang, *zhangfang2021@hit.edu.cn*

Abstract

Simplified assumptions of aerosol mixing states in modeling studies often introduce substantial uncertainties in estimating cloud condensation nuclei (CCN) concentrations (N_{CCN}) and their climatic impacts. This study systematically investigates the contrasting relationships between mixing states and CCN activity by combining field measurements of the hygroscopicity distribution with the algorithm of entropy at two inland and coastal sites. We show distinct seasonal variations of aerosol mixing state. In winter, externally-mixed particles dominated both sites, with comparable mixing state indices (χ) of 0.38±0.12 and 0.39±0.09 respectively for coastal air and inland air. However, measurements during summer periods showed pronounced differences: aerosols in the coastal atmosphere exhibited a higher degree of internal mixing (χ=0.69±0.19), whereas inland χ values only increased moderately to 0.47±0.12. Aerosol mixing state is largely influenced by primary emissions and secondary formation process. Externally-mixed particles originate chiefly from anthropogenic emissions in inland or sea salt in coastal. During the aging process, particles become more internally-mixed as the enhanced fraction of more-hygroscopic mode. A universal logarithmic correlation was identified between the critical diameter (D_{cri}) characterizing CCN activity and χ (D_{cri} = -32.15ln(χ)+84.71, Pearson r = -0.74), but with distinct decrement rates for coastal vs. inland aerosols. Further analysis reveals the covariation relationships between the mixing state and CCN activity: N_{CCN} exhibits heightened sensitivity to fluctuations in χ at low values. These results underscore that mixing states

exert different control over N_{CCN} in diverse environments. Our work provides critical constraints for parameterizing fine aerosols CCN activity in climate models.

1. Introduction

Atmospheric cloud condensation nuclei (CCNs) are complex mixtures of organic and inorganic components. Their chemical and physical properties make quantifying aerosol-cloud interactions challenging (Liu et al., 2018; Rosenfeld et al., 2019; Xu et al., 2022, 2024; Virtanen et al., 2025), introducing uncertainties into climate effect assessments (Charlson et al., 1992; Shrivastava et al., 2017; IPCC, 2021; Chen et al., 2022a; Manavi et al., 2025). Accurate climate model predictions of aerosol impacts require understanding aerosol mixing states under different atmospheric conditions and their effects on CCN activity (Ching et al., 2016; Zheng et al., 2021a). Current models often oversimplify mixing states by assuming pure internal or external mixing (Winkler, 1973; Stevens et al., 2019; Riemer et al., 2019; Zheng et al., 2021b). This is problematic because mixing states directly determine particle hygroscopicity distribution and CCN estimates (Wang et al., 2010; Tao et al., 2024). For example, internal-mixed aerosol particles have unimodal hygroscopicity distribution, while the external-mixed particles are characterized by the bimodal/trimodal or partly overlapping structures (Spitieri et al., 2023; Liu et al., 2025). Such simplifications can lead to significant errors, e.g., Sotiropoulou et al. (2007) found that mixing state assumptions caused two-fold N_{CCN} estimation errors in global models.

Systematic observations across diverse environments are critical because aerosol mixing states exhibit pronounced spatial-temporal variations (Ye et al., 2018; Hughes

et al., 2018; Liu et al., 2025). For example, continental and coastal regions present contrasting scenarios (Ramachandran et al., 2016). The continental areas are dominated by anthropogenic emissions, where aerosol aging is driven by industrial and traffic-related pollutants (Huang et al., 2014; Ren et al., 2023). Particles here undergo progressive internal mixing via photochemical process and heterogenous reactions, altering their hygroscopic properties (Ervens et al., 2010; Tao et al., 2021). While the coastal regions feature dynamic interactions between marine aerosols (e.g., sea salt) and continental pollutants (Schill et al., 2015; Collins et al., 2013; Cheung et al., 2020). Seasonal shifts in air mass sources (e.g., marine vs. continental dominance) might create unique mixing state patterns (Xu et al., 2020, 2021a). For instance, summer photochemical aging and heterogenous processes in coastal areas can enhance the degree of internal mixing, while winter often retains more external mixing due to the presence of the sea-salt particles with less-hygroscopic organic matter.

The continental aerosols influence regional cloud formation, while coastal aerosols may provide insights into the characteristics of marine aerosols in region. The properties of marine aerosols are significantly different from those of continental aerosols, and therefore have distinct climate feedback mechanisms (Bellouin et al., 2020; Xu et al., 2024; Liu et al., 2024). However, the current models lack regional-specific mixing state parameters and usually assume uniform mixing in both environments. This could lead to large uncertainties in predicting CCN concentrations, highlighting the need for site-specific observations. For example, Ren et al. (2018) found that the impact of aerosol mixing state on CCN activation characteristics ranged

from -34% to +16 % in urban atmosphere. Comparison between a fully internal mixture assumption and using the mixing state index from the particle-resolved model, Ching et al. (2017) found the obvious overestimation in CCN concentration estimation. Especially in the regions eg., Amazon Basin, Central Africa and Indonesia, the particles appeared to be more external, errors in CCN concentration would increase up to 100% (Hughes et al., 2018). A detailed exploration of mixing state on CCN concentration in global scale was conducted by Zheng et al. (2021a), and the results showed that the mixing state varied spatially with more externally mixed over the North Atlantic Ocean, off the coasts of Southern Africa, and Australia. Thus, assuming particles with internally-mixed would introduce errors in CCN concentration of 50-100%.

Therefore, for quantifying the aerosol mixing state in the ambient atmosphere, we apply the algorithm of entropy proposed by Riemer and West (2013) to investigate the aerosol heterogeneity. This index has been applied to quantify the mixing state more reasonably both in field campaigns (Zhao et al., 2021; Yuan et al., 2023) and model simulations (Ching et al., 2016; Zheng et al., 2021a). However, most studies focused on quantifying the particle heterogeneity in composition (Ching et al., 2019; Fierce et al., 2020; Zhao et al., 2021). Here we concentrated on evaluating the heterogeneity in aerosol hygroscopicity for sub-micron particles, which directly related to CCN budget. By refereeing to Yuan et al. 2023, the heterogeneity in hygroscopicity was investigated by combining in-situ measurements of probability distribution function of the hygroscopicity with the algorithm of entropy. Briefly, the mixing state index χ, is devised based on the concept of information entropy concerning the distribution of

hygroscopicity across the aerosol population. It varies between 0 (external mixing completely) and 1 (internal mixing completely). By integrating inland and coastal measurements, this study will focus on addressing two key gaps, (1) How continental vs. marine-dominated environments shape aerosol mixing states and CCN activity; (2) Whether χ-based CCN parameterizations show regional dependencies, providing critical constraints for climate models.

2. Data and Methods

2.1 Field Campaigns

The inland atmospheric measurements were conducted for two campaigns from 16 November to 6 December 2016 and 29 May to 13 June 2017 as a part of the Air Pollution and Human Health (APHH) project (Shi et al., 2019), at the Institute of Atmospheric Physics, Chinese Academy of Sciences (IAP, 39.97° N, 116.37° E) in urban Beijing. The campaigns were complemented by the hygroscopicity and CCN observations and were conducive to provide information on the aerosol hygroscopicity affecting urban pollutions. This urban site exhibited highly variable aerosol populations dominated by local anthropogenic sources including vehicular, cooking emissions, and residential heating. Coastal measurements were performed at the Mace Head atmospheric research station (MHD, 53.33° N, 9.90° W) from 1 November 2009 to 30 January 2010, and summer periods from 11 to 31 August 2009 and July 2010, which located on the west coast of Ireland. Aerosol particles here experience alternating influences from polluted continental and clean marine atmospheres. The map of the

sites was shown in Figure 1. More details about the campaigns were given in Fan et al. (2020) and Xu et al. (2021a).

Fig 1. Map of the sites in the Inland of the Institute of Atmospheric Physics (IAP) and Coastal of Mace Head (MHD). (© Google Maps, https://maps.google.com/, last access: 2 April 2025).

2.2 Instrumentation

Hygroscopicity measurements

The particle hygroscopicity at both sites was characterized using the humidified tandem differential mobility analyzer (HTDMA). The hygroscopic growth factor (Gf), defined as the ratio of the particle diameter at the fixed RH (90%) and dry diameter set in this study for 40, 80, 110, 150, 200 nm at IAP and 35, 50, 75, 110 and 165 nm at MHD, respectively. The RH calibration with ammonium sulfate for HTDMA system was given in Fig. S1. The Gf probability density function (Gf-PDF) was derived using the TDMAinv algorithm (Gysel et al., 2009). The number fraction (NF) of near-hydrophobic mode (NH: $Gf \leq 1.21$), and more hygroscopic mode (MH: $Gf > 1.21$) in IAP site was referred from Chen et al. (2022b). It was integrated into three modes for

150 the MHD site with the near-hydrophobic mode (NH: 1 < Gf < 1.3), more hygroscopic
151 mode (MH: 1.3 ≤ Gf < 1.85) and sea salt mode (SS: Gf ≥ 1.85) for further examination
152 (Xu et al., 2021a).

153 Here for each particle size, the hygroscopicity parameter κ can be subsequently
154 calculated using κ-Köhler theory (Petters and Kreidenweis, 2007):

155 $$\kappa = (Gf^3 - 1) \cdot \left[\frac{1}{RH}\exp\left(\frac{4\sigma_{\frac{s}{a}} M_w}{RT\rho_w D_d Gf}\right) - 1\right] \quad (1)$$

156 where RH is the HTDMA relative humidity (90% set in the instrument), $\sigma_{s/a}$ is the
157 surface tension of pure water (0.072 mN m^{-1}), M_w and ρ_w are the molecular weight and
158 the density of pure water, R is the gas constant, and T is the absolute temperature, D_d is
159 the droplet diameter.

160 Then, the κ-PDF is obtained and normalized as $\int_0^\infty c(\kappa)d\kappa = 1$, where $c(\kappa)$ is
161 normalized as κ-PDF. Further it was used to calculate the particle population
162 heterogeneity (Calculation seen in Section 2.3).

163 According to the κ-Köhler theory, the critical diameter (D_{cri}) corresponding to the
164 supersaturation ratio can be expressed as:

165 $$D_{cri} = \sqrt[3]{\frac{4A^3}{27\kappa ln^2 S}}\ ,\ A = \frac{4\sigma_{\frac{s}{a}} M_w}{RT\rho_w} \quad (2)$$

166 where S is the given supersaturation ratio (here 0.2% used in this study), κ is the mean
167 value of the hygroscopicity parameter calculated in Equation (1).

168 **Chemical components**

169 For the inland atmospheric measurements, the non-refractory submicron aerosol
170 (smaller than 1μm, NR-PM_1) chemical composition was quantitatively characterized
171 using the Aerodyne High-Resolution Time-of-Flight Aerosol Mass Spectrometer (HR-

ToF-AMS) (DeCarlo et al., 2006), including sulfate (SO_4^{2-}), nitrate (NO_3^-), ammonium (NH_4^+), chloride (Chl) and organics (Org). The black carbon (BC) mass concentration was determined from the light absorption with a seven-wavelength aethalometer (AE33, Magee Scientific Corp.).

Measurements of PM_1 in the coastal atmosphere were also performed by the HR-ToF-AMS, including major inorganic salts (non-sea-salt sulfate, nss-SO_4^{2-}; methanesulfonic acid, MSA; NO_3^-; NH_4^+) and organic matter. The sea salt was quantified using NaCl ion signal, which has been demonstrated in previous studies (Ovadnevaite et al., 2014). The instrument operation and calibration have been described in previous studies (Ovadnevaite et al., 2014; Xu et al., 2019).

Aerosol number size distribution and CCN number concentration

Particle number size distributions (PNSD) were measured using an integrated system consisting of a Differential Mobility Analyzer (DMA; model 3081, TSI Inc.) coupled with a Condensation Particle Counter (CPC; model 3772, TSI Inc.). During the measurements at IAP, the PNSD covered the size range of 10-550 nm with a 5-minute time resolution. It scanned size range of 20-500 nm at MHD with a 10-minute temporal resolution. The CCN number concentrations were quantified at both sites using a Droplet Measurement Technologies CCN counter (DMT-CCNc) (Lance et al., 2006). The instrument's supersaturation (SS) settings were carefully calibrated before and after each campaign using ammonium sulfate aerosol following Rose et al. (2008) (Fig. S1). Four effective supersaturations (SS) were 0.14%, 0.23%, 0.40% and 0.76% at IAP site. Four SS levels were 0.25%, 0.5%, 0.75% and 1% at MHD site with an uncertainty of

±0.03%. Using measurements at set supersaturation of 0.2% as an example explores the CCN activity in the following discussions.

2.3 Calculation the heterogeneity for aerosol particles

To characterize the heterogeneous distribution of the hygroscopic and non-hygroscopic components in populations (Chen et al., 2022b), we calculated the mixing state index (χ) using the κ-PDF, following the methodology of Yuan et al. (2023). Two surrogate groups in a population of N aerosol particles were assumed (Zheng et al., 2021a). One surrogate group consists the non- and/or slightly hygroscopic species with κ_N of <0.05 and another group contains the more hygroscopic species with κ_H of 0.5-0.6 (Yuan et al., 2023, referred inorganics). Ambient particles typically contain one or two of the components and the κ lies between 0 and 0.6 at IAP or 0.8 at MHD as shown in Figure S2. Taking into account the enhanced hydrophilicity of marine aerosols at MHD site, calculation assuming κ_H values of 0.7 and 0.8 were shown in Fig. S3. While these variations in κ_H introduced a mean uncertainty of 8% in χ values, it did not significantly affect the seasonal or site comparisons. The volume fraction of two surrogate groups can be calculated based on the total κ according to the Zdanovskii–Stokes–Robinson (ZSR) mixing rule (Zdanovskii, 1948; Stokes et al., 1966).

The mixing state index χ is defined as the affine ratio of the average particle species diversity ($D\alpha$) and population species diversity ($D\gamma$) as:

$$\chi = \frac{D_\alpha - 1}{D_\gamma - 1} \quad (3)$$

The average per-particle species diversity $D\alpha$ can be calculated as follows. First,

the mixing entropies at bin i (H_i) are determined according to equation (4),

$$H_i = -P_{i,N} \times lnP_{i,N} - P_{i,H} \times lnP_{i,H} \quad (4)$$

where $P_{i,N}$ and $P_{i,H}$ are the volume fraction of each group for the κ-PDF with X bins at bin i (i=1,2,…X), and can be determined from the $P_{i,N} + P_{i,H} = 1$ and $P_{i,N} \times \kappa_N + P_{i,H} \times \kappa_H = \kappa_i$. Here $\kappa_N = 0.01, \kappa_H = 0.6$; κ_i represents the hygroscopicity parameter at bin i.

Based on the assumption that particles in the same diameter have the same mixing entropy $H_\alpha = \sum_{j=1}^{N} P_j \times H_j$, $P_j = \frac{V_j}{V_{total}} = \frac{1}{N}$; the per-particle mixing entropies H_α is determined according to equation (5),

$$H_\alpha = \sum_{i=1}^{X} H_i \times c(\kappa)_i \times \Delta\kappa \quad (5)$$

where $c(\kappa)_i$ is the probability density of the normalized κ-PDF at bin i, and $\Delta\kappa$ represents the bin width. Then, the average per-particle species diversity $D\alpha$ can be determined as $D_\alpha = e^{H_\alpha}$;

The bulk population species diversity $D\gamma$ can be calculated as follows. First, the aerosol population of the mixing entropy can be calculated as equation (6):

$$H_\gamma = -P_N \times lnP_N - P_H \times lnP_H \quad (6)$$

where P_N and P_H are the volume fraction of the non-hygroscopic and hygroscopic components in the population, and can be calculated by equation (7) and (8):

$$P_N = \sum_{i=1}^{X} P_{i,N} \times c(\kappa)_i \times \Delta\kappa \quad (7)$$

$$P_H = \sum_{i=1}^{X} P_{i,H} \times c(\kappa)_i \times \Delta\kappa \quad (8)$$

Then, the bulk population species diversity $D\gamma$ can be determined as $D_\gamma = e^{H_\gamma}$. Here, the definition of surrogate species as supersets encompassing hygroscopicity

heterogeneity implies that the heterogeneity parameter χ ranges from 0 to 1. When the mixing index χ approaches 0, it indicates a completely segregated state where hygroscopic and non-hygroscopic species reside in distinct particles. While for the case the mixing index χ to be 1 represents that the non-hygroscopic and hygroscopic species distributing homogeneously throughout the aerosol population.

3. Result and Discussion

3.1 Comparison of the heterogeneity in the inland and coastal atmosphere

To characterize the hygroscopic heterogeneity of atmospheric aerosols, Figure 2 depicts variations in mixing state metrics (Dα, Dγ, χ) and the hygroscopic parameter (κ_{gf}) across particle size distributions. The Dα and χ decrease with increasing particle diameter, accompanied by higher κ_{gf} values at IAP site. This trend indicates that inland particle populations tend to homogenize into hygroscopic compositions through primary particle aging or secondary formation processes (Liu et al., 2025; Chen et al., 2022b; Zhong et al., 2022). In contrast, particles exhibit a non-monotonic pattern at MHD site: Dα and χ decrease for Aitken-mode particles (<100 nm) but increase for accumulation-mode particles. The κ_{gf} shows consistent size-dependent increases in both winter and summer campaigns.

Notably, the mixing state metrics exhibit a pronounced minimum at 75 nm particles, influenced by distinct mechanisms: winter minima reflect the high sea salt fraction, while summer minima are driven by anthropogenic organic matter (Cheung et al., 2020; Xu et al., 2021a). Lower winter χ values—coupled with broader κ-PDF

distributions—indicate stronger external mixing and compositional diversity compared to summer (Fig. S2). Seasonal χ and κ_{gf} disparities are more pronounced at MHD site, primarily driven by the seasonal alternation of marine and anthropogenic emission sources.

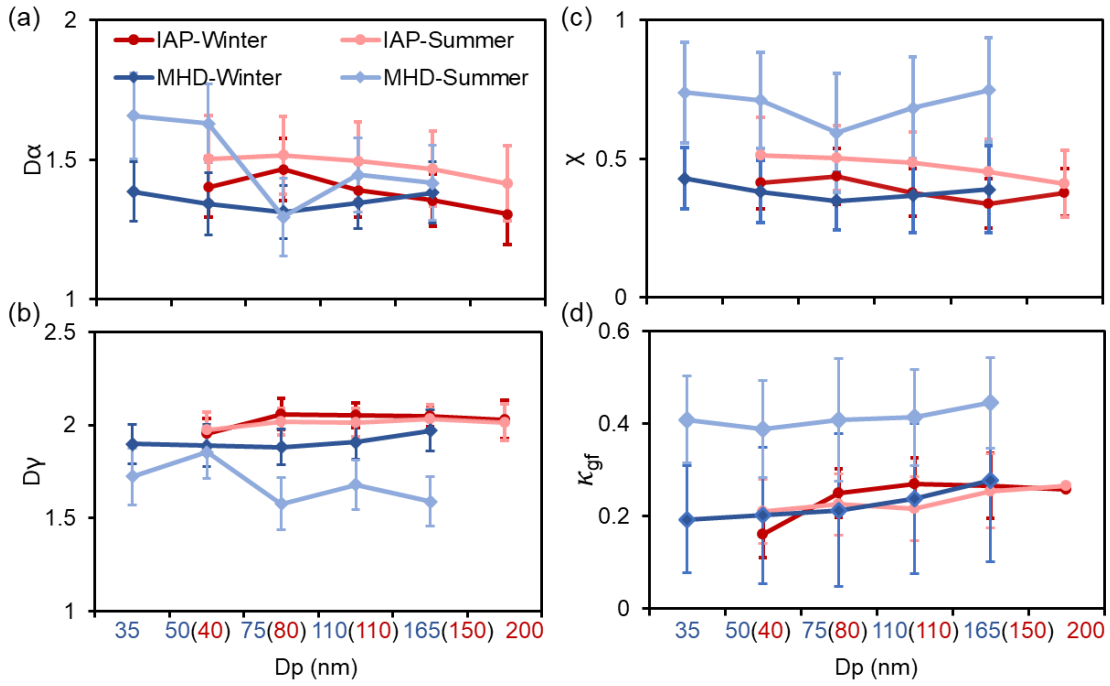

Fig 2. Mean values of the Dα (a), Dγ (b), χ (c) and κ_{gf} (d) for aerosols of five diameters during winter and summer periods at IAP and Mace Head sites.

Ultrafine particles (40 nm in IAP vs. 35 nm in MHD, Aitken mode) and larger particles (150 nm in IAP vs. 165 nm in MHD, accumulation mode) are selected to investigate distinct evolutionary processes of aerosol heterogeneity (Fig. 3 and Fig. S4). With the increasing of PM_1 concentration during winter, the variation in χ values exhibit only minor both at the IAP and MHD sites, generally fluctuating between approximately −0.04 and 0.08 (Fig. 3a and c). Inland accumulation-mode particles show a modest increase in χ, corresponding with a higher proportion of inorganic salts.

Conversely, at MHD site, the composition fraction shifts from a sea-salt dominance

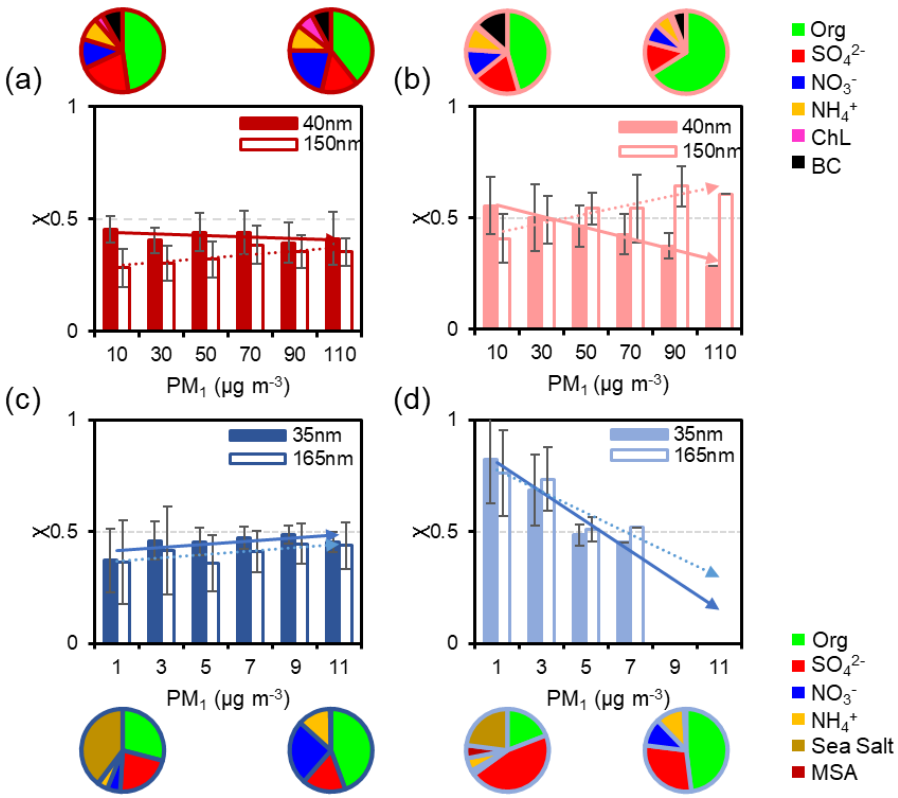

Fig 3. Variation of the average χ for 40 nm and 150 nm particles at IAP and 35 nm and 165 nm at MHD site with the particle mass concentration in IAP-winter (a), IAP-summer (b), MHD-winter (c) and MHD-summer (d). The pie charts represent the average mass fraction during four field measurements.

toward organic matter, accompanied by a ~20 % increase in nitrate content (Fig. 3c). In summer, the variation of χ with PM concentration becomes markedly pronounced at both IAP and MHD stations. For example, χ for 40 nm particles decreases as PM increases at IAP site (Fig. 3b). The elevated particle heterogeneity mainly arises from the locally primary emissions, corresponding to the enhanced primary organic emissions as shown in Fig. S5. It appeared more pronounced during evening rush hours. In contrast, χ for 150 nm particles increases from ~0.40 to ~0.60 with rising PM,

reflecting enhanced secondary formation and internal mixing during pollution process that render the particle population more homogeneous. At coastal sites, χ declines with rising PM by approximately 0.37 for 35 nm particles and 0.24 for 165 nm particles, mirroring the shift in chemical composition makeup from inorganic dominance to greater organic content (Fig. 3d).

Diurnal variations of mixing state metrics (Dα, Dγ, Gf-PDF and χ) at IAP and MHD sites are shown in Figure 4. In IAP-winter, particles exhibited steeper declines in Dα and χ during evening rush hours than summer, indicating a higher fraction of non-hygroscopic particles (40 nm) from fresh traffic emissions (Fig. 4a1 and S5). Concurrently, reduced Dγ values suggest that the bulk population consists of uniformly distributed less-hygroscopic (LH) components (Fig. 4c1). Aitken mode particles showed bimodal and broader Gf-PDF distributions, corresponding to cooking activities (11:00–13:00 LT) and traffic peaks (17:00–20:00 LT) (Cai et al., 2020). Midday photochemical aging promoted more internally mixed aerosols (Yang et al., 2012; Liu et al., 2025), as evidenced by increasing Dα at the urban site (Fig. 4b1). Conversely, the χ for accumulation-mode particles showed minimal diurnal variations both in IAP-winter and IAP-summer. This is mainly due to the dominant hygroscopic mode for 150 nm particles (Fig. 4g1 and 4h1), especially during summer, which is mainly from secondary formation or aging of the primary particles (such as the transformation from primary organic aerosol (POA) to secondary organic aerosol (SOA) in Fig. S5) (Wang et al., 2019; Fan et al., 2020).

For the coastal atmosphere, the mixing state metrics (Dα, Dγ, and χ) of Aitken and

accumulation mode particles in winter exhibited analogous diurnal patterns, characterized by a descending trend at nightfall (Fig. 4a2-h2). This corresponds to an enhanced modal distribution of near-hydrophobic (NH) particles at 35 nm and more-hygroscopic (MH) particles at 165 nm. In summer, Dα and Dγ both trended downward during daytime, with the decline of Dγ being more pronounced. A conspicuous seasonal discrepancy between Aitken and accumulation mode particles was observed in this region (Fig. 4a2–h2), where the mixing state index χ increased incrementally from winter to summer. Specifically, the mean χ for 35 nm particles escalated from 0.42 to 0.80, and for 165 nm particles, it rose from 0.39 to 0.76. This trend demonstrates a strong alignment with the spread factor (used as a measure of particle mixing state) documented by Xu et al. (2021a).

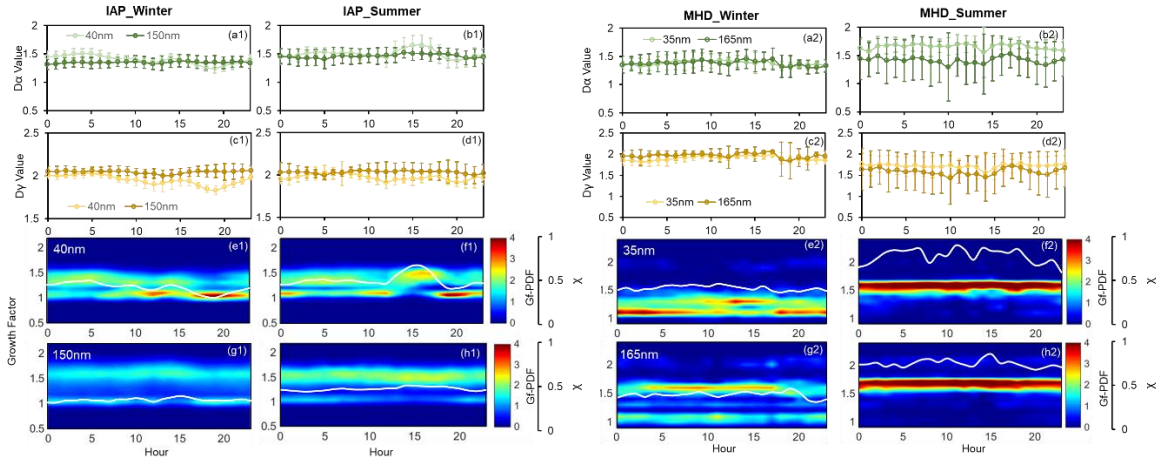

Fig 4. Diurnal variation of Dα, Dγ, Gf-PDF, and χ during winter and summer periods for 40 nm and 150 nm aerosols at IAP (a1-h1) and for 35 nm and 165 nm aerosols MHD site (a2-h2).

Similar to the mixing state χ, a very clear seasonal pattern of the aerosol

hygroscopic distribution was found (Fig. 4e-h). In winter, the Gf-PDF diurnal profiles of both Aitken and accumulation mode particles showed bimodal distribution (Fig. 4e2-g2) as evident by the number fraction of nearly-hydrophobic and more hygroscopic modes (Fig. S6). The NH mode is likely composed of anthropogenic organic matter and biogenic species derived from marine air masses (Xu et al., 2020), with this composition being particularly prominent in the Aitken mode. Additionally, Xu et al. (2021a) observed a higher abundance of the NH-mode in marine polar and Arctic air masses, this further supports the notion that NH particles are likely of biogenic origin, aside from contributions from anthropogenic activities. The more hygroscopic and sea salt mode was mostly contributed from the nss-sulfate and sea salt in winter (Xu et al., 2021a). Analogously, accumulation mode particles with a higher proportion of MH and SS mode (Fig. S6) primarily attributed to the prevalence of non-sea-salt sulfate (nss-sulfate) and sea salt in the coastal atmosphere (Xu et al., 2020). The bimodal and broad of hygroscopic distribution suggested that particles were more diverse and external mixed, consistent with the lower χ value in winter.

In contrast, summer observations revealed that Gf-PDFs of both Aitken and accumulation mode particles transitioned to unimodal distributions, signifying particles in summer had more homogeneous composition with a large extent of internal mixing particles (with higher χ). Such diurnal trend in Gf-PDFs was consistent along with the high number fraction of MH-mode and low NH-mode (Fig. S6). The higher hygroscopicity and MH mode in summer were largely driven by the enhancement of sulfate and decrease of organic matter (Fig. S6). And a clear shift from NH to MH mode

345 at midday might further demonstrate the promotion of photochemical aging in summer
346 (Xu et al., 2021a).

347 **3.2 Impacts of Primary Aerosol Emissions and Secondary Aerosol Formation on**
348 **Aerosol Mixing State**

349 As already noted above, changes in χ were clearly associated with the chemical
350 composition varying with site and season. The relationships between the mixing state
351 index and the number fraction of hydrophobic and hygroscopic mode during four
352 campaigns are presented in Figure S7. The χ exhibited negative correlations with the
353 fraction of hydrophobic mode but a positive relationship with the fraction of
354 hygroscopic particles, highlighting the markedly different effects of the primary
355 emissions and secondary formation on aerosol mixing state (Tao et al., 2024). To gain
356 more insight on this effect between inland and coastal atmosphere, four case are
357 analyzed (Fig. 5 and 6): case for IAP-winter, case for IAP-summer, case for MHD-
358 winter and case for MHD-summer.

359 Case for IAP-winter is a heavy polluted event with the mean PM mass
360 concentration increased from 22 to 437 μg m^{-3} (Fig. 5a-d). The 40- and 150-nm χ
361 patterns shifted quickly during the pollution periods. With the mass fraction of
362 hydrophobic compounds (ie., POA) in PM_1 increased, the χ of 40-nm particles
363 decreased from 0.5 to 0.2, that is, an enhanced NH mode and a weaken MH mode (Fig.
364 5b-c). At this stage, large particles for 150 nm are mainly from aqueous formation with
365 more proportion of nitrate. The corresponding χ of 150 nm was higher. While with that
366 the mass fractions of secondary organic and inorganic compositions increased, particles

were more internal mixed with χ increased to be 0.6 for 40-nm and 0.53 for 150-nm particles.

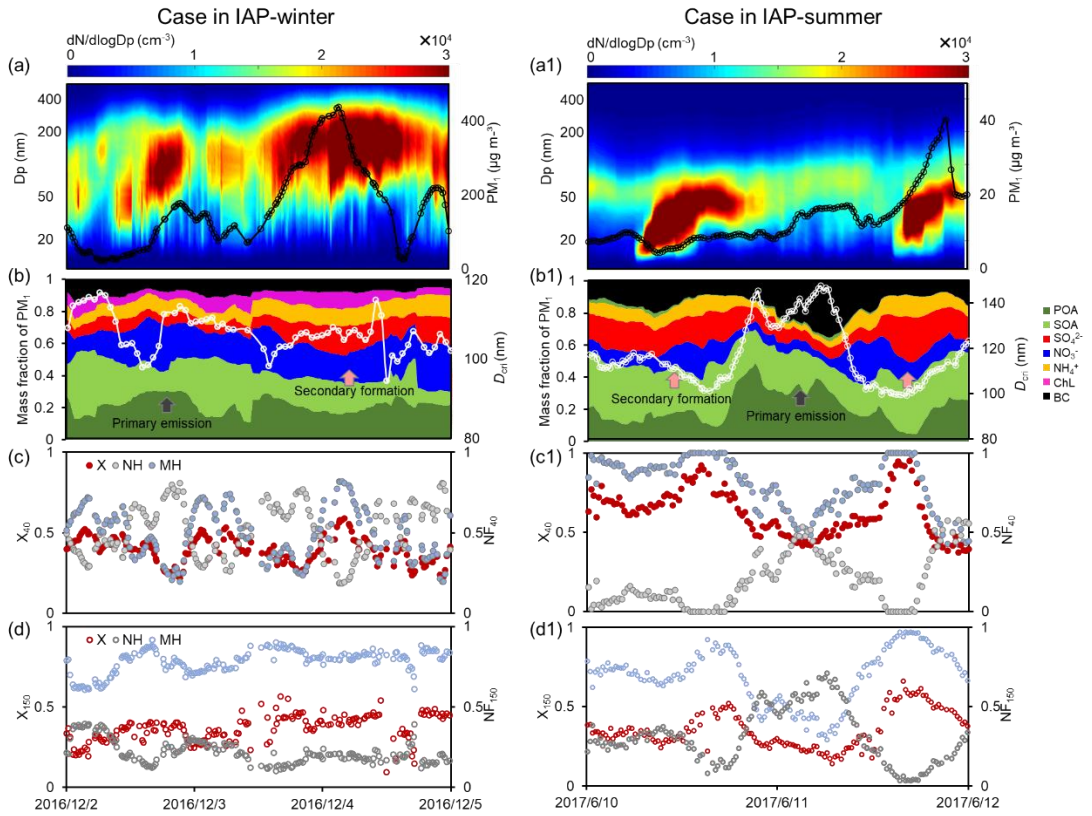

Fig 5. Case in IAP-winter (a-d) and IAP-summer (a1-d1). Particle number size distribution and PM_1 (a and a1), mass fraction of the PM_1 and the critical diameter (D_{cri}) (b and b1), mixing state index (χ), number fraction of the nearly hydrophobic mode (NH) and more hygroscopic mode (MH) for 40 nm particles (c and c1), χ, NH and MH for 150 nm particles (d and d1).

Case for IAP-summer is the typical new particle formation events (NPF) with the mean PM_1 of 13 μg m^{-3} (Fig. 5a1-d1). With the evolution of NPF events, the χ of 40- and 150-nm particles increased to be 0.95 and 0.61 with the enhanced proportion of more-hygroscopic components (ie., SOA, NO_3^-, SO_4^{2-}). The χ pattern is opposite of that

the number fraction of NH mode and consistent with the variation of MH mode (Fig. S7). Note that a sudden decrease in χ on June 11th was disturbed by the strong primary emission. The chemical mass fractions showed more POA and black carbon with an enhanced NH mode and a weaker MH mode (Fig. 5b1-d1). The χ of 40-nm particles decreased to be 0.4 and that of the 150-nm particles decreased to be 0.2. The χ patterns appear to similar transitions for Aitken and accumulation-mode particles during haze and NPF events. The increase in χ is synchronous with the increase in MH mode from secondary formation but opposite with that of LH mode from primary emissions. This implies that the primary emissions would lead particles more external mixing while secondary formation would promote aerosol more internal mixed in Inland atmosphere.

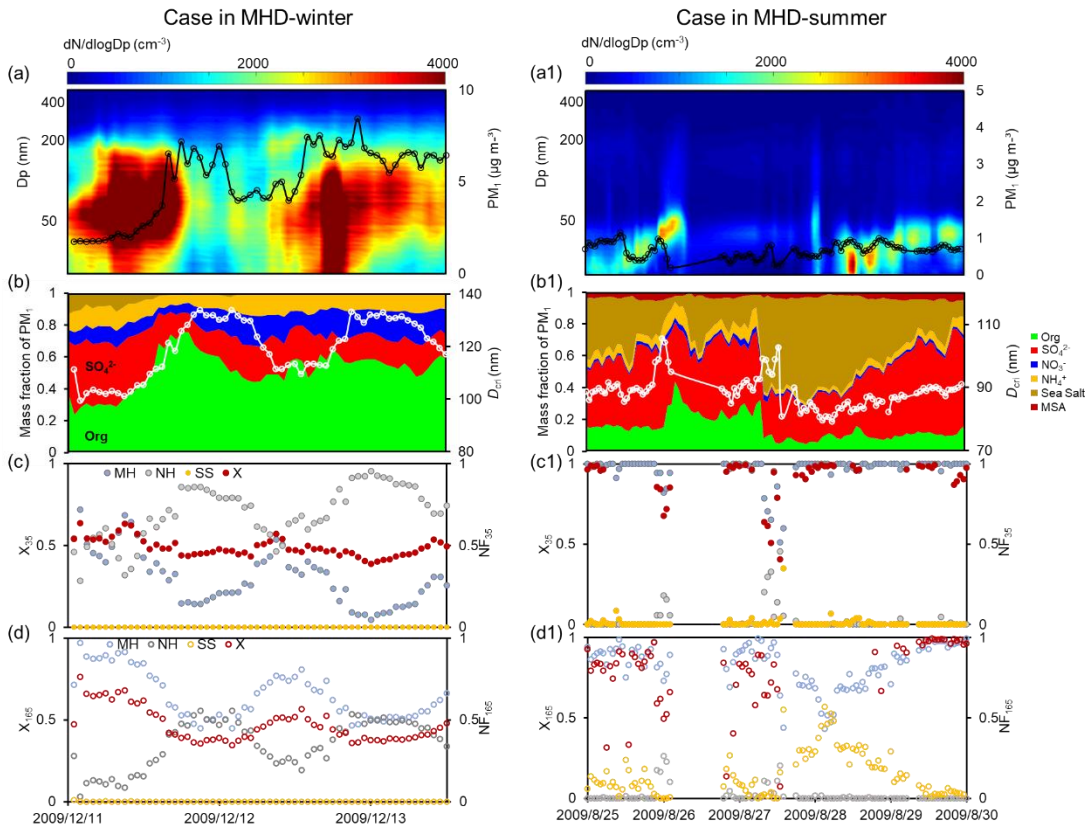

Fig 6. Case in MHD-winter (a-d) and MHD-summer (a1-d1). Particle number size distribution and PM_1 (a and a1), mass fraction of the PM_1 and the critical diameter (D_{cri})

392 (b and b1), mixing state index (χ), number fraction of the nearly hydrophobic mode
393 (NH) and more hygroscopic mode (MH) for 35 nm particles (c and c1), χ, NH and MH
394 for 165 nm particles (d and d1).

395 Case for MHD-winter is a high organic matter pollution event with the mean PM_1
396 of 5.2 μg m^{-3} and 52% mass fraction of organics (Fig. 6a-d). Larger presence of
397 anthropogenic organic matter resulted the NH mode for 35-nm particles to be 95% and
398 165-nm particles to be 53% (Fig. 6). The χ of 35- and 165-nm particles decreased with
399 the NH mode increased (Fig. S7), similar with the case for IAP site. There was a steady
400 increase in χ when the MH-mode particles started increasing with the increase in mass
401 fraction inorganics, eg., 35 nm particles showed the mean χ increasing from 0.43 to
402 0.57 and 165 nm particles from 0.35 to 0.6. This indicated that the trend of aerosol
403 mixing state closely followed the evolution emission and secondary formation.

404 Case for MHD-summer is an extremely clean event with the mean PM_1 of 0.7 μg
405 m^{-3} (Fig. 6a1-d1). The dominated MH mode was found throughout the case, which
406 could be attributed from the high mass fraction of nss-sulfate (41% average). Compared
407 with the case in MHD-winter, the mean proportion of organic has decreased to be 15%.
408 Therefore, the χ remains at a high value (mean χ of 0.9 for 35-nm and 0.8 for 165-nm
409 particles). Until August 28th, a stronger increase in the mass fraction of sea salt and
410 accordingly SS mode in larger-size particles was observed. The χ decreased rapidly
411 with the decrease in MH mode and enhanced SS mode, especially for the accumulation
412 mode particles, suggesting the sea spray production makes particles more externally
413 mixed.

In summary, these results suggest that the primary emission and secondary formation drive the hygroscopic distribution and can result in significant variation of aerosol mixing state χ both in Inland and coastal atmosphere. The pattern of χ varied among site and season, highlighting the importance of considering the impact of mixing state on CCN activity.

3.3 Covariation relationships between the Mixing State and CCN Activity

The mixing state of particle populations undergoes dynamic transformations during atmospheric aging, profoundly influencing their CCN activity. Unlike prior CCN closure studies that assumed mixing states based on chemical component fractions (Yang et al., 2012; Padró et al., 2012; Ren et al., 2018), this work employs the hygroscopicity distribution- and entropy-derived mixing state index χ to clarify the covariation relationships between the mixing state and CCN activity. Given that CCN activity reflects the characteristics of the entire particle population while χ is calculated from HTDMA measurements at specific particle diameters, this study chooses the N_{CCN}, activation ratio (AR) at supersaturation of 0.2% and the mean χ for accumulation-mode to illustrate the covariation characteristic approximately. This approach is employed to ensure that both variables/parameters reflect the characteristics of the accumulation-mode particle population. The covariations of particle size and chemical composition with the mixing state (χ ranging from 0 to 1 at intervals of 0.1) are illustrated in Figure 7. This figure provides key insights into two fundamental determinants of CCN activity (Dusek et al., 2006).

As χ increases, the peak diameter (D_{peak}) of the particle number size distribution (PNSD) shifts toward larger sizes (Fig. 7a and Fig. S8), while peak concentrations occur within the intermediate χ range (0.3–0.6). This trend indicates that CN number concentration (N_{CN}) first increases, driven by primary emissions and new particle formation, then decreases due to mixing and aging processes (Fig. 7b). Notably, new particle formation events frequently occurred in IAP-summer (Fig. S9), corresponding the gradually increase of χ. And the χ for Aitken-mode is significantly larger than the accumulation-mode particles during this period. Thus, N_{CN} exhibits a sustained slight increase as the degree of the internal mixing increases in IAP-summer.

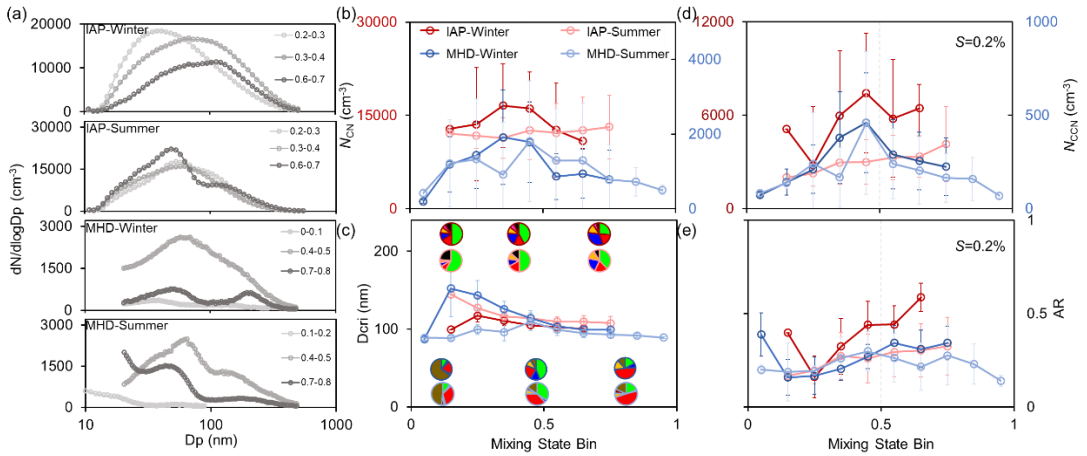

Fig 7. Comparison of the average particle number size distribution (PNSD) in different mixing state index (χ) (a), CN number concentration (N_{CN}) as a function of χ (b), Critical diameter (D_{cri}) at S=0.2% and mass fraction of chemical composition as a function of χ (c), CCN number concentration (N_{CCN}) (d) and activation ratio (AR) at S=0.2% a function of χ (e).

The critical diameter (D_{cri})—defined as the minimum size required for activation at a given supersaturation—depends on aerosol hygroscopicity. In turn, this

hygroscopicity is jointly determined by the hygroscopicity of individual soluble components and their mass fractions in the aerosol (Petters and Kreidenweis, 2007). Using measurements at supersaturation of 0.2% as an example, Fig. 7c shows that D_{cri} decreases with increasing highly hygroscopic inorganic components (e.g., sulfate, nitrate) in the inland atmosphere. In contrast, coastal D_{cri} exhibits nonlinear variations with χ: high external mixing (low χ) elevates D_{cri} due to dominant organic components, reducing sea salt particle fractions. As χ increases, the mass fraction of non-sea-salt sulfate (nss-sulfate) rises, enhancing activation potential by decreasing D_{cri}.

The covariation characteristic of CCN activity at 0.2% supersaturation with mixing state index χ reveals distinct inter-atmospheric differences, as shown in Fig. 7d-e. In IAP, N_{CCN} at S=0.2% demonstrates a monotonic increasing trend with χ, attributed to the synergistic effects of rising N_{CN} and decreasing D_{cri} (Fig. S10). By contrast, coastal N_{CCN} follows a pattern analogous to N_{CN}, with peak concentrations shifting toward higher χ values. This highlights the dominant role of particle size effects in enhancing CCN concentrations under marine-influenced conditions (Dusek et al., 2006).

Two distinct D_{cri}-χ trends underpin these disparities: one remains stable, driven by the inherent hygroscopicity of sea salt, while the other exhibits steep D_{cri} declines associated with anthropogenic pollution as internal mixing intensifies. These discrepancies are further manifested in the nonlinear D_{cri}-χ relationship. The activation ratio (AR)—quantifying aerosol cloud droplet formation potential at fixed supersaturation—also varies by site (Fig. 7e). Notably, AR shows a marked increase

with χ in IAP-winter, likely due to enhanced N_{CCN} from the elevated inorganic fraction under higher mixing states (Fig. 3). Conversely, the inorganic fraction decreases during other sampling periods, dampening AR growth.

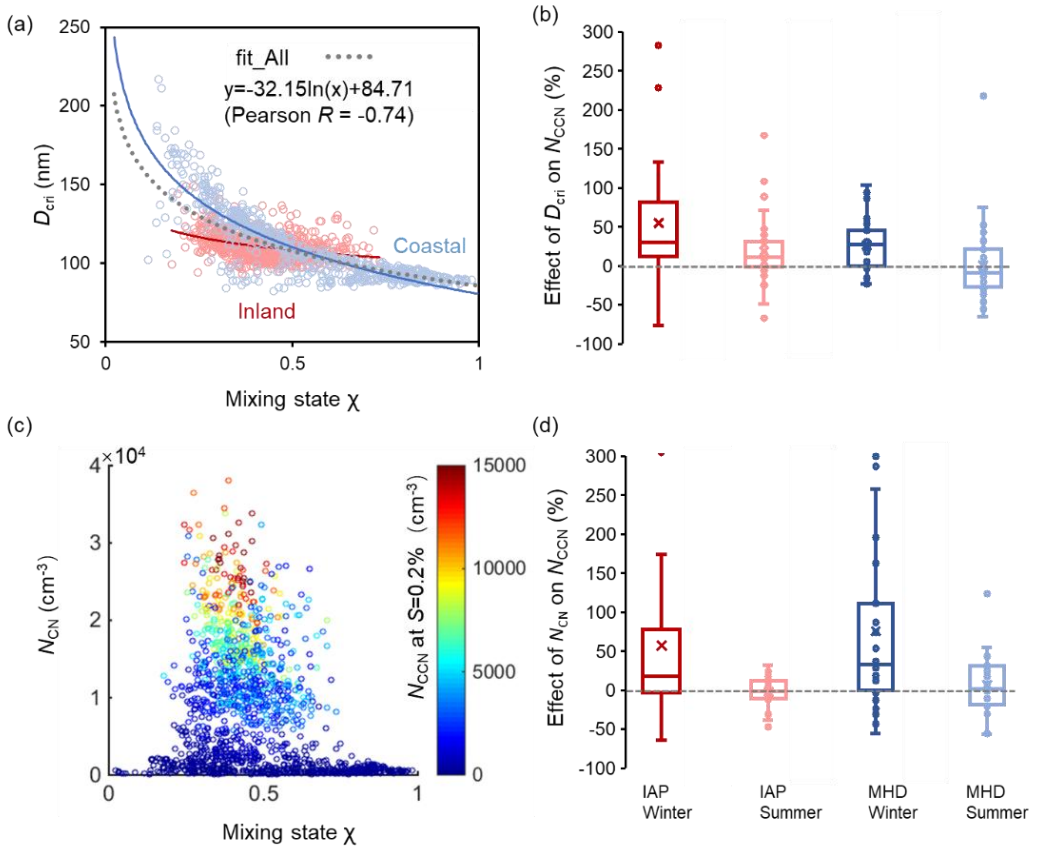

Fig 8. Covariation characteristics of the critical diameter (D_{cri}) with the χ (a), relative change of CCN number concentration (N_{CCN}) at supersaturation S = 0.2% with the reduction in D_{cri} (b); Covariation characteristics of the CN number concentration (N_{CN}) with the χ, different colors represent the N_{CCN} (c), relative change of N_{CCN} with the change in N_{CN} (d).

Fig. 8 further shows the covariation characteristics of CN concentration, chemical compositions (i.e., D_{cri}) with mixing state across particle populations. D_{cri} exhibits heightened sensitivity to minor χ fluctuations in the mixing state (χ) when χ < 0.5 (Fig.

8a). In contrast, for particles already characterized by internal mixing, further increases in χ (i.e., higher degrees of internal mixing) exert a negligible influence on D_{cri}. This behavior pattern implies that the D_{cri}-χ relationship could enable a novel parameterization for D_{cri} estimation, a framework that has not yet been reported in the existing literature.

Aerosol observation at MHD site (blue dots) span a broad D_{cri} range (80–220 nm) with χ varying from 0.1 to 1, reflecting alternating influences of highly hygroscopic inorganic salts (sea salt, sulfate) and less-hygroscopic organic matter. In contrast, aerosols—dominated by anthropogenic pollutants—exhibit a narrower D_{cri} range (90–150 nm) at IAP site. Both environments show negative D_{cri}-χ correlations, but with distinct functional forms: MHD aerosols feature an exceptional logarithmic fit (D_{cri} = -42.98ln(χ) +80.36, R^2 = 0.75; Fig. 8a blue line), while IAP aerosols (red line) yield a shallower slope (-12.04). Pooling all data, we derive a generalized parameterization: D_{cri} = -32.15ln(χ) + 84.71 (Pearson r = -0.74, R^2 = 0.54). As discussed above, strong impact of primary emission and secondary formation on aerosol mixing state was observed in both sites (Fig. 5 and 6). One could obtain more details on the D_{cri}-χ correlations. For example, the D_{cri} exhibited rapidly increase with the increase of primary emissions (ie., mass fraction of POA enhanced) during polluted periods. The D_{cri} pattern appeared opposite with that of the mixing state index, especially for the accumulation-mode particles. More pronounced D_{cri}-χ correlations were observed during the new particle formation (Fig. 5a1-d1). The decreasing presence of D_{cri} matched the increasing proportion of SO_4^{2-} and SOA with the χ increased during NPF

events. Similar correlations between the critical diameter and mixing state index were also found in the coastal atmosphere, especially for the case of the enhanced anthropogenic organic matter and sea salt production (Fig. 6). This implies that the relationship between the D_{cri} and χ might be disturbed by the variation of emission pollution and secondary formation processes, resulting in spatiotemporal differences. The D_{cri} reduces by 2.2–6.8% with the mixing state increase at a step of 0.1, with the steepest winter decline (Fig. S11).

Changes in N_{CN} with differ starkly between environments: positive effects in polluted inland air (+9%) versus negative effects in coastal regions (-2%). Aerosols in IAP, frequently perturbed by primary emissions and new particle formation, exhibit elevated N_{CN} (peaking at χ = 0.2–0.7), while in MHD N_{CN} remains ~5000 cm^{-3} across all χ. We categorized data into two groups: C1 (particles within specific N_{CN} ranges) evaluates N_{CCN} covariations mainly driven by D_{cri}-χ relationships, while C2 (particles within fixed D_{cri} intervals) assesses N_{CN}-χ effects (Fig. 8b). Relative changes (RC) in D_{cri}, N_{CN}, and N_{CCN} with χ were calculated by comparing successive χ increments (χi+1 vs. χi, i=0,0.1…1) within defined N_{CN} or D_{cri} windows.

Notably, the covariation relationship between the N_{CCN} and mixing state exerts more pronounced for the case of externally mixed aerosols dominated. For example, MHD-winter aerosols (high external mixing; χ_{mean}=0.38±0.12) showed RCs in N_{CCN} of 23% (C1) and 72% (C2), whereas MHD-summer aerosols (high internal mixing; χ_{mean}=0.69±0.19) exhibited negligible effects (-2.5% in C1, 0.9% in C2). Inland atmospheres, despite smaller seasonal χ variations, showed analogous trends: RCs of

530 N_{CCN} in winter (55% in C1, 57% in C2 for external mixing) exceeded summer values
531 for more internally mixed populations (Fig. 8d). These results confirm that hygroscopic
532 heterogeneity strongly influences N_{CCN} under external mixing, aligning with prior work
533 (Ching et al., 2017).

534 The covariation characteristics are most pronounced during winter in both
535 environments, attributed to heightened winter D_{cri} sensitivity to χ: a 0.1 χ increase
536 reduces D_{cri} by 5.2% (winter), boosting N_{CCN} by 39%, versus 2.4% D_{cri} reduction
537 (summer) yielding only 6% N_{CCN} enhancement. Concomitantly, winter N_{CN}-χ effects on
538 N_{CCN} reach 65%, far exceeding summer responses.

539 In contrast to previous evaluation methods that oversimplify mixing states (Ren et
540 al., 2018; Xu et al., 2021b), the entropy-based framework employed in this study
541 explicitly characterizes the covariation between the CCN activity and transitions in the
542 mixing state. Aerosols in IAP-winter are presumably shaped by intense urban pollution
543 sources—including traffic emissions, residential heating, and cooking activities—
544 thereby enriching the externally mixed particle fraction (Fan et al., 2020; Xie et al.,
545 2020). Analogously, aerosols in MHD-winter exhibit dominant external mixing,
546 consisting of near-hydrophobic and hydrophilic particle mixtures (Xu et al., 2021a). As
547 illustrated in Fig. S2, the winter aerosol population exhibits bimodal or multimodal κ–
548 PDF distributions—this pattern indicates a high degree of external mixing, with the
549 aerosols characterized by chemically diverse compositions. Collectively, these results
550 underscore the pivotal role of mixing state heterogeneity in modulating CCN activity
551 across different environments.

4. Conclusions

The mixing state of aerosol populations undergoes complex transformations during atmospheric aging, altering the distribution of hygroscopic and non-hygroscopic components and thus influencing CCN activity (Xu et al., 2021a; Ching et al., 2017). This study derived a mixing state index (χ) from field-measured hygroscopicity distributions, systematically investigating the covariation relationship between the mixing state and CCN activity at two inland and coastal environments. Results provide field evidence that aerosol mixing states generally reside between purely internal and external extremes (Chen et al., 2022b). Aerosol mixing state is largely influenced by the primary emissions and secondary formation process. Externally-mixed particles with more hydrophobic-mode originate chiefly from primary emissions in IAP, while that of more sea-salt mode from sea spray in MHD. While it becomes more internally-mixed as the enhanced fraction of more-hygroscopic mode and decreased of hydrophobic mode during the aging process. This highlights a dual regulatory mechanism of mixing state and its potential impact on hygroscopic distribution and CCN activity.

As χ increases, CN number concentrations (N_{CN}) first rise—driven by primary emissions and new particle formation—then decline due to condensation and coagulation during aging. Additionally, a logarithmic decreasing relationship between critical diameter (D_{cri}) and χ was identified for both inland and coastal particles, parameterized as $D_{cri} = -32.15\ln(\chi) + 84.71$ (Pearson $R = -0.74$, $R^2 = 0.54$). This offers a practical approach to estimate D_{cri} from χ, serving as a general framework for

integrating mixing state effects on CCN activity in atmospheric models.

Entropy-based analyses further support the covariation relationships between the mixing state and N_{CCN}, especially for externally mixed aerosols. Current models often oversimplify aerosol mixing states as purely internal or external (Stevens et al., 2019; Bauer et al., 2013), the latter being particularly sensitive to organic matter (Ren et al., 2018; Bhattu et al., 2015). Such simplifications introduce significant biases in N_{CCN} estimation (Riemer et al., 2019; Ching et al., 2019). The χ-D_{cri} parameterization proposed here offers a novel approach to reduce model complexity in representing aerosol hygroscopicity and CCN activation, enabling more accurate simulations of aerosol CCN capacity. It is expected mitigate the underestimation in CCN compared with the complete external mixing assumption, while effectively alleviates the overestimation that arises from applying the complete internal mixing assumption in regions characterized by high external mixing (Zheng et al., 2021a). This advancement improves our understanding of aerosol-cloud interactions (IPCC, 2021; Rosenfeld et al., 2019), critical for refining climate effect assessments.

Data availability

All data used in the study are available at https://doi.org/10.3974/geodb.2019.06.11.V1 (Fan et al., 2019) and http://doi.org/10.17632/3dx6pnx869.1 (Xu et al., 2021a).

Author contributions

RH and JR conceived the conceptual development of the paper. JR, FZ and WX directed and performed the experiments with YW and LC. FZ and YS provided the dataset in

the inland site. JO, DC and CO provided the dataset in the coastal site. JR conducted the data analysis and wrote the draft. All authors edited and commented on the various sections of the paper.

Competing interests

The contact author has declared that none of the authors has any competing interests.

Supporting Information

Additional analysis results that were applied in this study. Example of calibration results of HTDMA and CCN used in this study (Figure S1), mean values of the κ–PDF for aerosols of five diameters (Figure S2), sensitivity of the hygroscopic parameter for the group of the hygroscopic species on the mixing state index χ (Figure S3), time series of the average per-particle species diversity $D\alpha$, the bulk population species diversity $D\gamma$, and their affine ratio χ (Figure S4), diurnal trend of particle size, chemical mass fraction and number fraction (NF) of hydrophobic and hygroscopic mode in IAP (Figure S5) and in MHD (Figure S6), mixing state as a function of number fraction of hydrophobic and hygroscopic mode (Figure S7), variation of the peak diameter (D_{peak}) with the mixing state index (Figure S8), particle number size distribution and mixing state during new particle formation events (Figure S9), diurnal variation of χ and CN concentration during winter and summer periods for 40 nm and 150 nm aerosols in inland and for 35 nm and 165 nm aerosols in coastal site (Figure S10), relative change of the critical diameter and CN concentration with the mixing state index χ (Figure S11) (PDF).

Acknowledgements

This work was funded by the National Natural Science Foundation of China (NSFC) under Grant No. 42525301, 42405118 and 42475112, the State Key Laboratory of Loess Science, Institute of Earth Environment, Chinese Academy of Sciences (SKLLQG2429), the Guangdong Natural Science Foundation (Grant No. 2024A1515011005). We thank all participants of the field campaign for their hard work and sharing of the data.

References

Bhattu, D., Tripathi, S. N.: CCN closure study: Effects of aerosol chemical composition and mixing state, Journal of Geophysical Research: Atmospheres., 120(2), 766–783, https://doi.org/10.1002/2014JD021978, 2015.

Bellouin, N., Quaas, J., Gryspeerdt, E., Kinne, S., Stier, P., Watson-Parris, D., Boucher, O., Carslaw, K. S., Christensen, M., Daniau, A-L., Dufresne, J.-L., Feingold, G., Fiedler, S., Foster, P., Gettelman, A., Haywood, J. M., Lohmann, U., Malavelle, F., Mauritsen, T., McCoy, D. T., Schulz, M., Schwartz, S. E., Sourdeval, O., Storelvmo, T., Toll, V., Winker, D., and Stevens, B: Bounding global aerosol radiative forcing of climate change, Rev. Geophys., 58, e2019RG000660, https://doi.org/10.1029/2019RG000660, 2020.

Bauer, S. E., Ault, A., Prather, K. A.: Evaluation of aerosol mixing state classes in the GISS modelE-MATRIX climate model using single-particle mass spectrometry measurements, Journal of Geophysical Research: Atmospheres., 118, 9834–9844, https://doi.org/10.1002/jgrd.50700, 2013.

Charlson, R. J., Schwartz, S. E., Hales, J. M., Cess, R. D., Coakley Jr, J. A., Hansen, J. E., Hofmann, D. J.: Climate forcing by anthropogenic aerosols, Science., 255(5043), 423–430, https://doi.org/10.1126/science.255.5043.423, 1992.

Chen, Y., Haywood, J., Wang, Y., Malavelle, F., Jordan, G., Partridge, D., Fieldsend, J.,

642 Leeuw, J. D., Schmidt, A., Cho, N., Oreopoulos, L., Platnick, S., Grosvenor, D.,
643 Field, P., Lohmann, U.: Machine learning reveals climate forcing from aerosols is
644 dominated by increased cloud cover, Nature Geoscience., 15(8), 609–614,
645 https://doi.org/10.1038/s41561-022-01027-9, 2022a.
646 Chen, L., Zhang, F., Zhang, D., Wang, X., Song, W., Liu, J., Ren, J., Jiang, S., Li, X.,
647 and Li, Z.: Measurement report: Hygroscopic growth of ambient fine particles
648 measured at five sites in China, Atmospheric Chemistry and Physics., 22, 6773-
649 6786, https://doi.org/10.5194/acp-22-6773-2022, 2022b.
650 Ching, J., Zaveri, R. A., Easter, R. C., Riemer, N., Fast, J. D.: A three-dimensional
651 sectional representation of aerosol mixing state for simulating optical properties
652 and cloud condensation nuclei, Journal of Geophysical Research: Atmospheres.,
653 121(10), 5912–5929, https://doi.org/10.1002/2015JD024323, 2016.
654 Ching, J., Fast, J., West, M., Riemer, N.: Metrics to quantify the importance of mixing
655 state for CCN activity, Atmospheric Chemistry and Physics., 17(12), 7445–7458,
656 https://doi.org/10.5194/acp-17-7445-2017, 2017.
657 Ching, J., Adachi, K., Zaizen, Y., Igarashi, Y., Kajino, M.: Aerosol mixing state revealed
658 by transmission electron microscopy pertaining to cloud formation and human
659 airway deposition, npj Climate and Atmospheric Science., 2(1), 22, https://doi.org/
660 10.1038/s41612-019-0081-9, 2019.
661 Collins, D. B., Ault, A. P., Moffet, R. C., Ruppel, M. J., Cuadra-Rodriguez, L. A.,
662 Guasco, T. L., Corrigan, C. E., Pedler, B. E., Azam, F., Aluwihare, L. I., Bertram,
663 T. H., Roberts, G. C., Grassian, V. H., Prather, K. A.: Impact of marine
664 biogeochemistry on the chemical mixing state and cloud forming ability of nascent
665 sea spray aerosol, Journal of Geophysical Research: Atmospheres., 118(15), 8553–
666 8565, https://doi.org/10.1002/jgrd.50598, 2013.
667 Cheung, H. C., Chou, C. C. K., Lee, C. S. L., Kuo, W. C., Chang, S. C.: Hygroscopic
668 properties and cloud condensation nuclei activity of atmospheric aerosols under
669 the influences of Asian continental outflow and new particle formation at a coastal
670 site in eastern Asia, Atmospheric Chemistry and Physics., 20(10), 5911–5922,

https://doi.org/10.5194/acp-20-5911-2020, 2020.

Cai, J., Chu, B., Yao, L., Yan, C., Heikkinen, L. M., Zheng, F., Li, C., Fan, X., Zhang, S., Yang, D., Wang, Y., Kokkonen, T. V., Chan, T., Zhou, Y., Dada, L., Liu, Y., He, H., Paasonen, P., Kujansuu, J. T., Petäjä, T., Mohr, C., Kangasluoma, J., Bianchi, F., Sun, Y., Croteau, P. L., Worsnop, D. R., Kerminen, V. M., Du, W., Kulmala, M., & Daellenbach, K. R.: Size-segregated particle number and mass concentrations from different emission sources in urban Beijing, Atmospheric Chemistry and Physics., 20(21), 12721–12740, https://doi.org/10.5194/acp-20-12721-2020, 2020.

Dusek, U., Frank, G. P., Hildebrandt, L., Curtius, J., Schneider, J., Walter, S., Chand, D., Drewnick, F., Hings, S., Jung, D., Borrmann, S., Andreae, M. O.: Size matters more than chemistry for cloud-nucleating ability of aerosol particles, Science., 312 (5778), 1375−1378, https://doi.org/10.1126/science.1125261, 2006.

DeCarlo, P. F., Kimmel, J. R., Trimborn, A., Northway, M. J., Jayne, J. T., Aiken, A. C., Gonin, M., Fuhrer, K., Horvath, T., Docherty, K. S., Worsnop, D. R., Jimenez, J. L.: Field-deployable, high-resolution, time of-flight aerosol mass spectrometer, Analytical Chemistry., 78, 8281–8289, https://doi.org/10.1021/ac061249n, 2006.

Ervens, B., Cubison, M. J., Andrews, E., Feingold, G., Ogren, J. A., Jimenez, J. L., Quinn, P. K., Bates, T. S., Wang, J., Zhang, Q., Coe, H., Flynn, M., Allan, J. D.: CCN predictions using simplified assumptions of organic aerosol composition and mixing state: a synthesis from six different locations, Atmospheric Chemistry and Physics., 10(10), 4795–4807, https://doi.org/10.5194/acp-10-4795-2010, 2010.

Fierce, L., Onasch, T. B., Cappa, C. D., Mazzoleni, C., China, S., Bhandari, J., Davidovits, P., Fischer, D. A., Helgestad, T., Lambe, A. T., et al.: Radiative absorption enhancements by black carbon controlled by particle-to-particle heterogeneity in composition, P. Natl. Acad. Sci. USA, 117, 5196–5203, https://doi.org/10.1073/pnas.1919723117, 2020.

Fan, X., Liu, J., Zhang, F., Chen, L., Collins, D., Xu, W., Jin, X., Ren, J., Wang, Y., Wu, H., Li, S., Sun, Y., Li, Z.: Contrasting size-resolved hygroscopicity of fine particles derived by HTDMA and HR-ToF-AMS measurements between summer and

winter in Beijing: the impacts of aerosol aging and local emissions, Atmospheric Chemistry and Physics., 20(2), 915–929, https://doi.org/10.5194/acp-20-915-2020, 2020.

Gysel, M., Mcfiggans, G. B., Coe, H.: Inversion of tandem differential mobility analyser (TDMA) measurements, Journal of Aerosol Science., 40(2), 134–151, https://doi.org/10.1016/j.jaerosci.2008.07.013, 2009.

Hughes, M., Kodros, J. K., Pierce, J. R., West, M., Riemer, N.: Machine learning to predict the global distribution of aerosol mixing state metrics, Atmosphere., 9(1), 15, https://doi.org/10.3390/atmos9010015, 2018.

Huang, R. J., Zhang, Y., Bozzetti, C., Ho, K. F., Cao, J. J., Han, Y., Daellenbach, K. R., Slowik, J. G., Platt, S. M., Canonaco, F., Zotter, P., Wolf, R., Pieber, S. M., Bruns, E. A., Crippa, M., Ciarelli, G., Piazzalunga, A., Schwikowski, M., Abbaszade, G., Schnelle-Kreis, J., Zimmermann, R., An, Z., Szidat, S., Baltensperger, U., Haddad, I. E., Prévôt, A. S.: High secondary aerosol contribution to particulate pollution during haze events in China, Nature., 514(7521), 218–222, https://doi.org/10.1038/nature13774, 2014.

IPCC. Summary for Policymakers. In Climate Change 2021: The Physical Science Basis. Contribution of Working Group I to the Sixth Assessment Report of the Intergovernmental Panel on Climate Change; Cambridge University Press: Cambridge, United Kingdom and New York, NY, USA, 2021.

Liu, P., Song, M., Zhao, T., Gunthe, S. S., Ham, S., He, Y., Qin, Y., Gong, Z., Amorim, C. J., Bertram, K. A., Martin, S. T.: Resolving the mechanisms of hygroscopic growth and cloud condensation nuclei activity for organic particulate matter, Nature communications., 9(1), 4076, https://doi.org/10.1038/s41467-018-06622-2, 2018.

Liu, J., Zhang, F., Ren, J., Chen, L., Zhang, A., Wang, Z., Zou, S., Xu, H., Yue, X.: The evolution of aerosol mixing state derived from a field campaign in Beijing: implications for particle aging timescales in urban atmospheres, Atmospheric Chemistry and Physics., 25(9), 5075–5086, https://doi.org/10.5194/acp-25-5075-

2025, 2025.

Liu, Y., Lin, T., Zhang, J., Wang, F., Huang, Y., Wu, X., Ye, H., Zhang, G., Cao, X., and de Leeuw, G.: Opposite effects of aerosols and meteorological parameters on warm clouds in two contrasting regions over eastern China, Atmospheric Chemistry and Physics., 24, 4651–4673, https://doi.org/10.5194/acp-24-4651-2024, 2024.

Lance, S., Nenes, A., Medina, J., Smith, J. N.: Mapping the operation of the DMT continuous flow CCN counter, Aerosol Science and Technology., 40(4), 242–254, https://doi.org/10.1080/02786820500543290, 2006.

Manavi, S. E. I., Aktypis, A., Siouti, E., Skyllakou, K., Myriokefalitakis, S., Kanakidou, M., Pandis, S. N.: Atmospheric aerosol spatial variability: Impacts on air quality and climate change, One Earth., 8(3), https://doi.org/10.1016/j.oneear.2025.101237, 2025.

Ovadnevaite, J., Ceburnis, D., Leinert, S., Dall'Osto, M., Canagaratna, M., O'Doherty, S., Berresheim, H., O'Dowd, C.: Submicron NE Atlantic marine aerosol chemical composition and abundance: Seasonal trends and air mass categorization, Journal of Geophysical Research: Atmospheres., 119, 11850–11863, https://doi.org/10.1002/2013JD021330, 2014.

Petters, M. D., Kreidenweis, S. M.: A single parameter representation of hygroscopic growth and cloud condensation nucleus activity, Atmospheric Chemistry and Physics., 7(8), 1961–1971, https://doi.org/10.5194/acp-7-1961-2007, 2007.

Padró, L. T., Moore, R. H., Zhang, X., Rastogi, N., Weber, R. J., and Nenes, A.: Mixing state and compositional effects on CCN activity and droplet growth kinetics of size-resolved CCN in an urban environment, Atmospheric Chemistry and Physics., 2012, 12, 10239–10255, https://doi.org/10.5194/acp-12-10239-2012, 2012.

Rosenfeld, D., Zhu, Y., Wang, M., Zheng, Y., Goren, T., Yu, S.: Aerosol- driven droplet concentrations dominate coverage and water of oceanic low-level clouds, Science., 363(6427), https://doi.org/10.1126/science. aay4194, 2019.

Riemer, N., Ault, A. P., West, M., Craig, R. L., Curtis, J. H.: Aerosol mixing state: Measurements, modeling, and impacts, Reviews of Geophysics., 57(2), 187–249, https://doi.org/10.1029/2018RG000615, 2019.

Ren, J., Zhang, F., Wang, Y., Collins, D., Fan, X., Jin, X., Xu, W., Sun, Y., Cribb, M., Li, Z.: Using different assumptions of aerosol mixing state and chemical composition to predict CCN concentrations based on field measurements in urban Beijing, Atmospheric Chemistry and Physics., 18(9), 6907–6921, https://doi.org/10.5194/acp-18-6907-2018 2018.

Ramachandran, S., Srivastava, R.: Mixing states of aerosols over four environmentally distinct atmospheric regimes in Asia: coastal, urban, and industrial locations influenced by dust, Environmental Science and Pollution Research., 23, 11109–11128, https://doi.org/10.1007/s11356-016-6254-8, 2016.

Ren, J., Zhang, F., Chen, L., Cao, G., Liu, M., Li, X., Wu, H., Cheng, Y., and Li, Z.: Identifying the hygroscopic properties of fine aerosol particles from diverse sources in urban atmosphere and the applicability in prediction of cloud nuclei, Atmos. Environ., 298, 119615, https://doi.org/10.1016/j.atmosenv.2023.119615, 2023.

Riemer, N. and West, M.: Quantifying aerosol mixing state with entropy and diversity measures, Atmospheric Chemistry and Physics., 13, 11423–11439, https://doi.org/10.5194/acp-13-11423-2013, 2013.

Rose, D., Gunthe, S. S., Mikhailov, E., Frank, G. P., Dusek, U., Andreae, M. O., Pöschl, U.: Calibration and measurement uncertainties of a continuous-flow cloud condensation nuclei counter (DMT-CCNC): CCN activation of ammonium sulfate and sodium chloride aerosol particles in theory and experiment, Atmospheric Chemistry and Physics., 8(5), 1153–1179, https://doi.org/10.5194/acp-8-1153-2008, 2008.

Shrivastava, M., Cappa, C. D., Fan, J., Goldstein, A. H., Guenther, A. B., Jimenez, J. L., Kuang, C., Laskin, A., Martin, S. T., Ng, N. L., Petaja, T., Pierce, J. R., Rasch, P. J., Roldin, P., Seinfeld, J. H., Shilling, J., Smith, J. N., Thornton, J. A., Volkamer,

R., Wang, J., Worsnop, D. R., Zaveri, R. A., Zelenyuk, A., Zhang, Q.: Recent advances in understanding secondary organic aerosol: Implications for global climate forcing, Reviews of Geophysics., 55(2), 509–559, https://doi.org/10.1002/2016RG000540, 2017.

Stevens, R., and Dastoor, A.: A Review of the Representation of Aerosol Mixing State in Atmospheric Models, Atmosphere., 10, 168, https://doi.org/10.3390/atmos10040168, 2019.

Spitieri, C., Gini, M., Gysel-Beer, M., and Eleftheriadis, K.: Annual cycle of hygroscopic properties and mixing state of the suburban aerosol in Athens, Greece, Atmospheric Chemistry and Physics., 23, 235–249, https://doi.org/10.5194/acp-23-235-2023, 2023.

Sotiropoulou, R. E. P., Nenes, A., Adams, P. J., Seinfeld, J. H.: Cloud condensation nuclei prediction error from application of Köhler theory: Importance for the aerosol indirect effect, Journal of Geophysical Research: Atmospheres., 112(D12), https://doi.org/10.1029/2006JD007834, 2007.

Schill, S. R., Collins, D. B., Lee, C., Morris, H. S., Novak, G. A., Prather, K. A., Quinn, P. K., Sultana, C. M., Tivanski, A. V., Zimmermann, K., Cappa, C. D., Bertram, T. H.: The impact of aerosol particle mixing state on the hygroscopicity of sea spray aerosol, ACS central science., 1(3), 132-141, https://doi.org/10.1021/acscentsci.5b00174, 2015.

Shi, Z., Vu, T., Kotthaus, S., Harrison, R. M., Grimmond, S., Yue, S., Zhu, T., Lee, J., Han, Y., Demuzere, M., Dunmore, R. E., Ren, L., Liu, D., Wang, Y., Wild, O., Allan, J., Acton, W. J., Barlow, J., Barratt, B., Beddows, D., Bloss, W. J., Calzolai, G., Carruthers, D., Carslaw, D. C., Chan, Q., Chatzidiakou, L., Chen, Y., Crilley, L., Coe, H., Dai, T., Doherty, R., Duan, F., Fu, P., Ge, B., Ge, M., Guan, D., Hamilton, J. F., He, K., Heal, M., Heard, D., Hewitt, C. N., Hollaway, M., Hu, M., Ji, D., Jiang, X., Jones, R., Kalberer, M., Kelly, F. J., Kramer, L., Langford, B., Lin, C., Lewis, A. C., Li, J., Li, W., Liu, H., Liu, J., Loh, M., Lu, K., Lucarelli, F., Mann, G., McFiggans, G., Miller, M. R., Mills, G., Monk, P., Nemitz, E., O'Connor,

F., Ouyang, B., Palmer, P. I., Percival, C., Popoola, O., Reeves, C., Rickard, A. R., Shao, L., Shi, G., Spracklen, D., Stevenson, D., Sun, Y., Sun, Z., Tao, S., Tong, S., Wang, Q., Wang, W., Wang, X., Wang, X., Wang, Z., Wei, L., Whalley, L., Wu, X., Wu, Z., Xie, P., Yang, F., Zhang, Q., Zhang, Y., Zhang, Y., and Zheng, M.: Introduction to the special issue "In-depth study of air pollution sources and processes within Beijing and its surrounding region (APHH-Beijing)", Atmospheric Chemistry and Physics., 19, 7519–7546, https://doi.org/10.5194/acp-19-7519-2019, 2019.

Stokes, R. H., Robinson, R. A.: Interactions in aqueous nonelectrolyte solutions. I. Solute-Solvent equilibria, Journal of Physical Chemistry., 70(7), 2126–2130, https://doi.org/10.1021/j100879a010, 1966.

Tao, J., Kuang, Y., Ma, N., Hong, J., Sun, Y., Xu, W., Zhang, Y., He, Y., Luo, Q., Xie, L., Su, H., and Cheng, Y.: Secondary aerosol formation alters CCN activity in the North China Plain, Atmospheric Chemistry and Physics., 21, 7409–7427, https://doi.org/10.5194/acp-21-7409-2021, 2021.

Tao, J., Luo, B., Xu, W., Zhao, G., Xu, H., Xue, B., Zhai, M., Xu, W., Zhao, H., Ren, S., Zhou, G., Liu, L., Kuang, Y., and Sun, Y.: Markedly different impacts of primary emissions and secondary aerosol formation on aerosol mixing states revealed by simultaneous measurements of CCNC, H(/V)TDMA, and SP2, Atmospheric Chemistry and Physics., 24, 9131–9154, https://doi.org/10.5194/acp-24-9131-2024, 2024.

Virtanen, A., Joutsensaari, J., Kokkola, H., Partridge, G. D., Blichner, S., Seland, Ø., Holopainen, E., Tovazzi, E., Lipponen, A., Mikkonen, S., Leskinen, A., Hyvärinen, A., Zieger, P., Krejci, R., Ekman, A. M. L., Riipinen, I., Quaas, J., Romakkaniemi, S.: High sensitivity of cloud formation to aerosol changes, Nature Geoscience., 1–7, https://doi.org/10.1038/s41561-025-01662-y, 2025.

Winkler, P.: The growth of atmospheric aerosol particles as a function of the relative humidity—II. An improved concept of mixed nuclei, Journal of Aerosol Science., 4(5), 373–387, https://doi.org/10.1016/0021-8502(73)90027-X, 1973.

Wang, J., Cubison, M. J., Aiken, A. C., Jimenez, J. L., Collins, D. R.: The importance of aerosol mixing state and size-resolved composition on CCN concentration and the variation of the importance with atmospheric aging of aerosols, Atmospheric Chemistry and Physics., 10(15), 7267–7283, https://doi.org/10.5194/acp-10-7267-2010, 2010.

Wang, Y., Li, Z., Zhang, R., Jin, X., Xu, W., Fan, X., et al.: Distinct ultrafine- and accumulation-mode particle properties in clean and polluted urban environments, Geophysical Research Letters., 46, 10,918–10,925, https://doi.org/10.1029/2019GL084047, 2019.

Xu, W., Ovadnevaite, J., Fossum, K. N., Lin, C., Huang, R. J., Ceburnis, D., O'Dowd, C.: Sea spray as an obscured source for marine cloud nuclei, Nature Geoscience., 15(4), 282–286, https://doi.org/10.1038/s41561-022-00917-2, 2022.

Xu, W., Ovadnevaite, J., Fossum, K. N., Huang, R. J., Huang, D., Zhong, H., Gu, Y., Lin, C., Huang, C., O'Dowd, C., Ceburnis, D.: Condensation of organic-inorganic vapours governs the production of ultrafine secondary marine cloud nuclei, Communications Earth & Environment., 5(1), 359, https://doi.org/10.1038/s43247-024-01519-z, 2024.

Xu, W., Ovadnevaite, J., Fossum, K. N., Lin, C., Huang, R. J., O'Dowd, C., Ceburnis, D.: Aerosol hygroscopicity and its link to chemical composition in the coastal atmosphere of Mace Head: marine and continental air masses, Atmospheric Chemistry and Physics., 20(6), 3777–3791, https://doi.org/10.5194/acp-20-3777-2020, 2020.

Xu, W., Ovadnevaite, J., Fossum, K. N., Lin, C., Huang, R.-J., O'Dowd, C., Ceburnis, D.: Seasonal trends of aerosol hygroscopicity and mixing state in clean marine and polluted continental air masses over the Northeast Atlantic, Journal of Geophysical Research: Atmospheres., 126, e2020JD033851, https://doi.org/10.1029/2020JD033851, 2021a.

Xu, W., Sun, Y., Wang, Q., Zhao, J., Wang, J., Ge, X., Xie, C., Zhou, W., Du, W., Li, J., Fu, P., Wang, Z., Worsnop, D. R., Coe, H.: Changes in aerosol chemistry from

2014 to 2016 in winter in Beijing: Insights from high-resolution aerosol mass spectrometry, Journal of Geophysical Research: Atmospheres., 124, 1132–1147, https://doi.org/10.1029/2018JD029245, 2019.

Xie, C., He, Y., Lei, L., Zhou, W., Liu, J., Wang, Q., Xu, W., Qiu, Y., Zhao, J., Sun, J., Li, L., Li, M., Zhou, Z., Fu, P., Wang, Z., Sun, Y.: Contrasting mixing state of black carbon-containing particles in summer and winter in Beijing, Environmental Pollution., 263, 114455, https://doi.org/10.1016/j.envpol.2020.114455, 2020.

Xu, W., Fossum, K. N., Ovadnevaite, J., Lin, C., Huang, R. J., O'Dowd, C., Ceburnis, D.: The impact of aerosol size-dependent hygroscopicity and mixing state on the cloud condensation nuclei potential over the north-east Atlantic, Atmospheric Chemistry and Physics., 21(11), 8655–8675, https://doi.org/10.5194/acp-21-8655-2021, 2021b.

Ye, Q., Gu, P., Li, H. Z., Robinson, E. S., Lipsky, E. M., Kaltsonoudis, C., Lee, A. K. Y., Apte, J. S., Robinson, A. L., Sullivan, R. C., Presto, A. A., Donahue, N. M.: Spatial variability of sources and mixing state of atmospheric particles in a metropolitan area, Environmental Science & Technology., 52, 6807–6815, https://doi.org/10.1021/acs.est.8b01011, 2018.

Yuan, L., and Zhao, C.: Quantifying particle-to-particle heterogeneity in aerosol hygroscopicity, Atmospheric Chemistry and Physics., 23, 3195–3205, https://doi.org/10.5194/acp-23-3195-2023, 2023.

Yang, F., Chen, H., Du, J., Yang, X., Gao, S., Chen, J., Geng, F.: Evolution of the mixing state of fine aerosols during haze events in Shanghai, Atmospheric Research., 104: 193-201, https://doi.org/10.1016/j.atmosres.2011.10.005, 2012.

Zheng, Z., Curtis, J. H., Yao, Y., Gasparik, J. T., Anantharaj, V. G., Zhao, L., West, M., Riemer, N.: Estimating submicron aerosol mixing state at the global scale with machine learning and Earth system modeling, Earth and Space Science., 8(2), e2020EA001500, https://doi.org/10.1029/2020EA001500, 2021a.

Zheng, Z., West, M., Zhao, L., Ma, P.-L., Liu, X., and Riemer, N.: Quantifying the structural uncertainty of the aerosol mixing state representation in a modal model,

902 Atmospheric Chemistry and Physics., 21, 17727–17741,
903 https://doi.org/10.5194/acp-21-17727-2021 , 2021b.
904 Zhao, G., Tan, T., Zhu, Y., Hu, M., and Zhao, C.: Method to quantify black carbon
905 aerosol light absorption enhancement with a mixing state index, Atmospheric
906 Chemistry and Physics., 21, 18055–18063, https://doi.org/10.5194/acp-21-18055-
907 2021, 2021.
908 Zdanovskii, A.: New methods for calculating solubilities of electrolytes in
909 multicomponent systems, Zh. Fiz. Khim. C, 22, 1475–1485, 1948.
910 Zhong, H., Huang, R. J., Lin, C., Xu, W., Duan, J., Gu, Y., Huang, W., Ni, H.; Zhu, C.,
911 You, Y., Wu, Y., Zhang, R., Ovadnevaite, J., Ceburnis, D., O'Dowd, C.:
912 Measurement report: On the contribution of long-distance transport to the
913 secondary aerosol formation and aging, Atmospheric Chemistry and Physics., 22,
914 9513–9524, https://doi.org/10.5194/acp-22-9513-2022, 2022.